X-ray and SZ constraints on the properties of hot CGM

Priyanka Singh,[1]⋆ Subhabrata Majumdar,[2] Biman B. Nath[3] and Joseph Silk[4,5,6]

[1]*Inter-University Centre for Astronomy and Astrophysics, Ganeshkhind, Post Bag 4, Pune 411007, India*
[2]*Tata Institute of Fundamental Research, Mumbai 400005, India*
[3]*Raman Research Institute, Bangalore 560080, India*
[4]*Institut d'Astrophysique de Paris (UMR 7095: CNRS & UPMC – Sorbonne Universités), 98 bis bd Arago, F-75014 Paris, France*
[5]*Department of Physics and Astronomy, The Johns Hopkins University Homewood Campus, Baltimore, MD 21218, USA*
[6]*BIPAC, Department of Physics, University of Oxford, Keble Road, Oxford OX1 3RH, UK*

ABSTRACT

We use observations of stacked X-ray luminosity and Sunyaev–Zel'dovich (SZ) signal from a cosmological sample of $\sim$80 000 and 104 000 massive galaxies, respectively, with $10^{12.6} \lesssim M_{500} \lesssim 10^{13}$ M$_\odot$ and mean redshift, z $\sim$ 0.1–0.14 to constrain the hot circumgalactic medium (CGM) density and temperature. The X-ray luminosities constrain the density and hot CGM mass, while the SZ signal helps in breaking the density–temperature degeneracy. We consider a simple power-law density distribution ($n_e \propto r^{-3\beta}$) as well as a hydrostatic hot halo model, with the gas assumed to be isothermal in both cases. The data sets are best described by the mean hot CGM profile $\propto r^{-1.2}$, which is shallower than an NFW profile. For halo virial mass $\sim 10^{12} - 10^{13}$ M$_\odot$, the hot CGM contains $\sim$ 20–30 per cent of galactic baryonic mass for the power-law model and 4–11 per cent for the hydrostatic halo model, within the virial radii. For the power-law model, the hot CGM profile broadly agrees with the observations of the Milky Way. The mean hot CGM mass is comparable to or larger than the mass contained in other phases of the CGM for $L*$ galaxies.

Key words: galaxies: haloes – X-rays: galaxies.

1 INTRODUCTION

The evidence for the absence of a significant fraction of baryons, otherwise predicted by the Λ–CDM cosmological model, covers a large number of observations (e.g. Klypin, Zhao & Somerville 2002; Bell et al. 2003; Flynn et al. 2006; Anderson & Bregman 2010; McGaugh et al. 2010; Miller & Bregman 2015). This lack of the baryons, also known as the 'galactic missing baryons problem', becomes severe as one goes down to the range of galactic masses. Analytical as well as numerical studies have indicated the existence of a hot (T $>10^6$ K) and diffuse circumgalactic medium (CGM), occupying the galactic halo (Rees & Ostriker 1977; Silk 1977; White & Frenk 1991; Maller & Bullock 2004; Kereš et al. 2005; Crain et al. 2010; Sharma et al. 2012). Recent observations of the Milky Way and other massive galaxies also support the presence of a significant fraction of galactic baryons in the hot phase of CGM (e.g. Grcevich & Putman 2009; Anderson & Bregman 2011; Dai et al. 2012; Gatto et al. 2013). Previous estimates from stacking of $\sim$2000 galaxies yielded hot CGM masses of $1.5-3.3\times 10^{10}$ M$_\odot$ within 200 kpc (Anderson, Bregman & Dai 2013). The hot CGM is also predicted to be detectable through its Sunyaev–Zel'dovich (SZ) and X-ray power spectra using the combination of high-resolution surveys such as South Pole Telescope, the extended Roentgen Survey with an Imaging Telescope Array, and the Dark Energy Survey (Singh et al. 2015, 2016). Other phases of CGM such as warm (T $\sim 10^5 - 10^6$ K), cool (T $\sim 10^4 - 10^5$ K), and the cold (T $< 10^4$ K) phases are also expected to contribute significantly to the total amount of CGM. However, there is considerable uncertainty in the knowledge of total CGM mass, contribution of different CGM phases, and their density profiles (e.g. Tumlinson, Peeples & Werk 2017).

In this paper, we constrain the properties of hot CGM using the stacked soft (0.5–2keV) X-ray emission detected down to $M_* \sim 6 \times 10^{10}$ M$_\odot$ by Anderson et al. (2015; hereafter, A15) and stacked thermal SZ (tSZ) signal detected down to $M_* \sim 10^{11}$ M$_\odot$ by the Planck Collaboration XI (2013; hereafter, P13). We aim to obtain a simple analytical model of the hot gas distribution for galaxies ($M_v \sim 10^{12} - 10^{13}$ M$_\odot$), which can explain the above measurements consistently. To our knowledge, it is the first study combining stacked tSZ and X-ray measurements to constrain CGM properties focused on the galaxy mass regime. We do not attempt to fit the full mass range observed by P13 and A15, whose data include those of galaxy clusters and groups. A single characterization of hot gas is not expected in such different classes of objects.

⋆ E-mail: priyankas@iucaa.in

2 DATA SETS

In this section, we describe the data sets used here and the physical processes underlying tSZ effect and X-ray emission.

2.1 Thermal SZ effect

It has been difficult to detect tSZ signal from galaxies due to their small gas reservoir. However, this situation can be improved upon by stacking a large number of galaxies thus increasing the signal-to-noise ratio (SNR).

P13 stacked *Planck* tSZ signal from a large number ($\sim 2.5 \times 10^5$) of locally brightest galaxies (LBGs), and divided into 20 logarithmically equally spaced stellar mass bins. They detected the stacked signal with SNR > 3σ at $M_* > 2 \times 10^{11}$ M$_\odot$ ($M_{500}{}^1 > 2 \times 10^{13}$ M$_\odot$), whereas the stacked signal is marginally detected (SNR ~ 1.6–2.6σ) down to $M_* \sim 10^{11}$ M$_\odot$ ($M_{500} \sim 4 \times 10^{12}$ M$_\odot$). The LBG sample is obtained after applying a series of selection criteria on New York University Value Added Galaxy Catalogue based on SDSS–DR7 (see P13 for details of the selection criteria). The selection criteria ensure that each galaxy in the sample is central to its dark matter halo. The stellar mass of each LBG is obtained from SDSS photometry (Blanton & Roweis 2007). In order to connect the stellar mass to the host dark matter halo properties, P13 use a mock galaxy catalogue created by Millennium Simulation, which is tuned to mimic the SDSS galaxy catalogue (Springel et al. 2005; Guo et al. 2013).

The stacked tSZ signal, Y_{500}, is the Compton y-parameter integrated over the sphere of radius R_{500}:

$$Y_{500} = \frac{\sigma_T}{m_e c^2 D_A^2(z)} \int_0^{R_{500}} P_e dV, \tag{1}$$

where D_A is the angular diameter distance, $P_e = n_e k_b T_e$ is the electron pressure, n_e and T_e are electron density and temperature, respectively. Instead of dealing directly with Y_{500}, the results are shown in terms of $\tilde{Y}_{500}$, which is the tSZ signal scaled to $z = 0$ and to a fixed angular diameter distance. It is related to Y_{500} as

$$\tilde{Y}_{500} \equiv Y_{500} E^{-2/3}(z)(D_A(z)/500\text{Mpc})^2. \tag{2}$$

P13 do not directly measure $\tilde{Y}_{500}$ due to the large beam size of *Planck*. Instead, they measure cylindrically integrated tSZ signal within a much larger aperture of size $5R_{500}$, which is given by

$$Y_{cyl} = \frac{\sigma_T}{m_e c^2 D_A^2(z)} \int_0^{5R_{500}} 2\pi r dr \int_r^{5R_{500}} \frac{2 P_e(r') r' dr'}{\sqrt{r'^2 - r^2}}. \tag{3}$$

The cylindrical tSZ signal, Y_{cyl}, is then converted into Y_{500} assuming a pressure profile of the gas. P13 assume that the gas follows universal pressure profile (Arnaud et al. 2010) to convert Y_{cyl} to Y_{500}. The conversion factor (Y_{cyl}/Y_{500}) is close to two for the universal pressure profile (Greco et al. 2015; Le Brun, McCarthy & Melin 2015). However, this conversion factor may vary significantly for different pressure profiles and halo masses (Greco et al. 2015). Therefore, it is appropriate to compare the results for other gas distributions with cylindrical tSZ signal. In this paper, we use equation (3) to compute $\tilde{Y}_{cyl}$ for other pressure profiles and then compare our predictions directly with the measurements of cylindrical tSZ signal.

2.2 X-ray emission

The hot phase of CGM also manifests itself in X-rays due to its high temperature. A15 stacked X-ray luminosity of LBGs in the soft X-ray band (0.5–2keV) of *ROSAT* all sky survey, thus detecting X-ray emission from the hot gas down to $M_* \sim 10^{10.8}$ M$_\odot$. Additionally, they measured X-ray emission arising only from region $(0.15-1) \times R_{500}$, referring it as the circumgalactic emission. They start with the same sample of LBGs as used by P13 and apply additional selection criteria (see Section 3.1 and fig. 1 of A15), thus producing a slightly smaller sample of LBGs. A15 estimated the effective halo mass, M_{500}, for 12 highest stellar mass bins of the sample using their best-fitting L_X–M_{500} relation, whereas P13 used their Y_{500}–M_{500} relation with Arnaud et al. (2010) pressure profile to get M_{500}. The difference between the two is small. The LBGs span a redshift range $\sim 0.1-0.14$ in the mass range of interest. We summarize both data sets in the mass range of our interest in Table 1. The uncertainties quoted in the table (and used in this work) are bootstrap errors and the mean redshift is computed from the mean luminosity distances. We use *WMAP7* cosmology throughout this paper. Analytically, the X-ray luminosity of the hot CGM ($0.15R_{500}$ to R_{500}) can be computed using the following relation:

$$L_X^{CGM} = \int_{0.15R_{500}}^{R_{500}} 2\pi r dr \int_r^{R_{500}} \frac{2 n_e n_i \Lambda(Z, T_e) r' dr'}{\sqrt{r'^2 - r^2}}, \tag{4}$$

where Z is the CGM metallicity, n_i is the proton density, and $\Lambda(Z, T_e)$ is the cooling function. We use the Astrophysical Plasma Emission Code (APEC; Smith et al. 2001) to calculate $\Lambda(Z, T)$. We fix the CGM metallicity at $Z = 0.2$ (Li et al. 2017) for our main results and explore the effects of a different metallicity in Section 4.3. Similar to tSZ results, we scale the X-ray luminosity to $z = 0$, denoted by $\tilde{L}_X^{CGM} = L_X^{CGM} E^{-7/3}(z)$.

3 CGM DENSITY AND TEMPERATURE

We use Markov chain Monte Carlo (MCMC)[2] analysis to determine the CGM density and temperature. We explore the following two spherical gas distributions.

3.1 A power-law model

First, we consider a simple power-law density profile given by $n_e(r) \propto r^{-3\beta}$. The power-law density profile is equivalent to a standard β-model at radii larger than the core radius. The gas fraction f_{gas} (i.e. the ratio of gas mass within the virial radius R_v and the total halo virial mass M_v[3]) is given by

$$f_{gas} = \frac{4\pi \mu_e m_p}{M_v} \int_0^{R_v} dr\, r^2 n_e(r), \tag{5}$$

where μ_e ($= 1.36$) is the mean molecular mass per electron. We assume the gas to be isothermal (to keep the model simple and reduce the number of free parameters), at temperature f_T times the virial temperature of the halo, i.e. $T_{gas} = f_T \times T_v$, where

$$T_{vir} = \frac{\mu\, m_p G M_v}{2k_b R_v}. \tag{6}$$

Here, μ ($= 0.59$, for primordial ionized gas) is the mean molecular weight of the gas. We then use f_{gas} and f_T to define the free

---

[1]Mass enclosed within a radius R_{500} such that the mean density is 500 times the critical density of the Universe.

[2]MCMC; Foreman-Mackey et al. 2013.

[3]We define the virial mass and virial radius in terms of overdensity, $\Delta_c(z) = 18\pi^2 + 82(\Omega_M(z) - 1) - 39(\Omega_M(z) - 1)^2$.

Table 1. Summary of tSZ and X-ray data sets used here.

$\log M_*$	$\log M_{500}$ ($M_\odot$)	$\tilde{Y}_{500} \pm \sigma \tilde{Y}_{500}$	$\log L_X^{CGM} \pm \sigma L_X^{CGM}$	z	Number of LBGs stacked
$M_\odot$	P13 (A15)	10^{-6}arcmin^2	log erg s^{-1}		P13 (A15)
11.15	12.97 (13.09)	1.7 ± 1.0	40.99 ± 0.11	0.135	22 085 (18 430)
11.05	12.71 (12.91)	1.27 ± 0.78	40.55 ± 0.53	0.127	26 026 (21 583)
10.95	12.62 (12.75)	1.54 ± 0.60	40.28 ± 0.48	0.113	28 325 (22 689)
10.85	12.40 (12.60)	$-$	39.28 ± 0.93	0.105	27 866 (22 490)
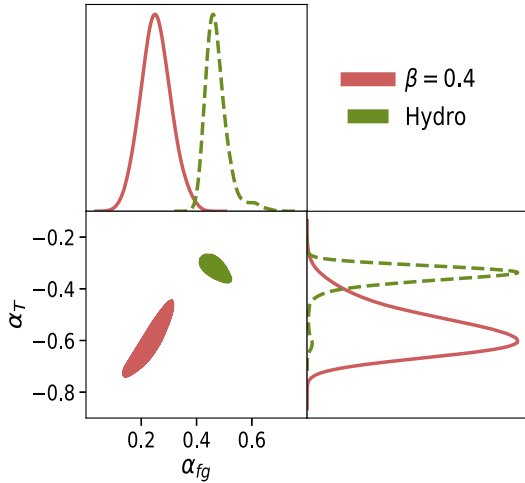
Figure 1. The 68 per cent CL contours for α_{fg} and α_T computed using MCMC. The solid (red) lines and contour correspond to the power-law model, whereas the dashed (green) lines and contour correspond to hydrostatic hot halo model.

parameters of our model, namely α_{fg} and α_T, given by

$$f_{gas} = \frac{\Omega_B}{\Omega_M}\left(\frac{M_v}{10^{15}M_\odot}\right)^{\alpha_{fg}}$$
$$f_T = f_{12}\left(\frac{M_v}{10^{12}M_\odot}\right)^{\alpha_T}. \qquad (7)$$

The functional form of f_{gas} is inspired from the observed deficit of hot gas in lower mass systems compared to the massive haloes (Bell et al. 2003; McGaugh et al. 2010), with the hot gas mass being close to the cosmic baryon fraction in the clusters. We use MCMC analysis to constrain α_{fg} and α_T. For both parameters, we use uniform priors large enough that they do not affect the results of the fitting process. GETDIST PYTHON package[4] is used to analyse and plot the results of MCMC analysis.

There are two more free parameters f_{12} (the value of f_T at $M_v = 10^{12}$ M$_\odot$) and β in the formalism described above. The observed temperature of the hot gas in the Milky Way (Miller & Bregman 2015) and external galaxies with $M_v \gtrsim 10^{12}$ M$_\odot$ (Li et al. 2017) is generally $\gtrsim 2 \times 10^6$K. Therefore, we fix $f_{12} \sim 3.4$ (for the above mentioned definition of virial temperature). We find that the reduced-$\chi^2 \rightarrow 1$ for $\beta = 0.4$. A flatter gas distribution ($\beta < 0.4$) gives a bad fit to the data (reduced-$\chi^2 > 1$), whereas a steeper gas distribution ($\beta > 0.4$) overfits the data sets (reduced-$\chi^2 < 1$). Therefore, we fix $\beta = 0.4$ for the rest of the analysis.

In Fig. 1, we show the one and two-dimensional projections of model parameters' posterior probability distribution and their 68 per cent confidence limit (CL) contours. The best-fitting values of the model parameters are represented by the mean of posterior

distribution, whereas their uncertainties are represented by the one-dimensional 68 per cent CL (see Table 2).

For the power-law model, we obtain $\alpha_{fg} = 0.24 \pm 0.061$ that translates to $f_{gas} \sim 3.2^{+1.7}_{-1.1}$ per cent and $5.5^{+1.8}_{-1.4}$ per cent (i.e. a baryon budget of ~ 20 per cent and 30 per cent) for virial masses $M_v = 10^{12}$ and 10^{13} M$_\odot$, respectively. The hot CGM fraction increases to 7.7 (13) per cent at $M_v = 10^{12}$ (10^{13}) M$_\odot$, i.e. a baryon budget of 46 (78) per cent, if the same gas density profile is extrapolated out to $2R_v$. The best-fitting value of $\alpha_T = -0.59^{+0.071}_{-0.12}$ compensates for the increasing virial temperature with virial mass, giving $T_{gas} \sim 0.21^{+0.04}_{-0.05}$ keV at $M_v \sim 10^{13}$ M$_\odot$. The constraints on α_{fg} and hence hot gas fraction are driven by the X-ray measurements as the X-ray luminosity is highly sensitive to the underlying gas distribution. However, X-ray emission weakly depends on the gas temperature thus giving poor constraints on α_T. On the other hand, tSZ is degenerate between gas density and temperature. Combining tSZ with X-ray breaks this degeneracy and the constraints on α_T are primarily driven by tSZ, which favours a lower gas temperature as both hot and warm gases contribute to the tSZ signal.

3.2 Isothermal hydrostatic equilibrium

Next, we explore an isothermal distribution of the hot CGM in hydrostatic equilibrium with the dark matter halo with the gas density profile given by

$$n_e(r) \propto \exp\left[-\left(\frac{\mu m_p G M_v}{k_b T_{gas} R_s}\right)\frac{1 - \log(1 + r/R_s)/(r/R_s)}{\log(1 + C_v) - C_v/(1 + C_v)}\right], \qquad (8)$$

where $R_s (\equiv R_v/C_v)$ is the scale radius and C_v is the concentration parameter of the dark matter halo (Duffy et al. 2008). The hot gas fraction and the temperature are determined by equation (7).

A hydrostatic model (reduced-$\chi^2 \approx 0.64$) prefers a higher value of α_{fg} and hence a lower gas fraction. The best-fitting value of $\alpha_{fg} \sim 0.48^{+0.027}_{-0.051}$ predicts $f_{gas} \sim 0.6^{+0.3}_{-0.1}$ per cent and $1.8^{+0.5}_{-0.2}$ per cent (i.e. a baryon budget of 4 per cent and 11 per cent) for the virial masses $M_v = 10^{12}$ and 10^{13} M$_\odot$, respectively. At the same time, the gas temperatures are higher (i.e. a lower value of α_T) than a simple power-law gas distribution. The best-fitting value of $\alpha_T \sim -0.33^{+0.052}_{-0.023}$ gives $T_{gas} \sim 0.38^{+0.05}_{-0.02}$ keV at $M_v = 10^{13}$ M$_\odot$. The main difference between the power-law and the hydrostatic equilibrium model is that the temperature of the hydrostatic model directly affects its gas density profile (see equation 8). Hydrostatic equilibrium tries to keep the gas temperature close to the virial temperature and a higher temperature leads to a lower gas fraction. Extrapolating the density profile out to $2R_v$ gives $f_{gas} \sim 2.2$ (4) per cent at $M_v = 10^{12}$ (10^{13}) M$_\odot$, i.e. a baryon budget of ~ 13 (24) per cent.

In Fig. 2, we compare the stacked CGM X-ray luminosity and the tSZ measurements with the predictions of our best-fitting models along with their 68 per cent uncertainty region. The power-law model predicts a larger X-ray and tSZ signal throughout the mass range considered except near the upper mass end, where the hy-

Table 2. X-ray–tSZ joint constraints from MCMC analysis.

Model	α_{fg} (Mean $\pm$ 68 per cent CL)	α_T (Mean $\pm$ 68 per cent CL)	f_{gas} ($10^{12} M_\odot$)	f_{gas} ($10^{13} M_\odot$)
$\beta = 0.4$	0.24 ± 0.061	$-0.59^{+0.071}_{-0.12}$	$3.2^{+1.7}_{-1.1}$ per cent	$5.5^{+1.8}_{-1.4}$ per cent
Hydro	$0.48^{+0.027}_{-0.051}$	$-0.33^{+0.052}_{-0.023}$	$0.6^{+0.3}_{-0.1}$ per cent	$1.8^{+0.5}_{-0.2}$ per cent
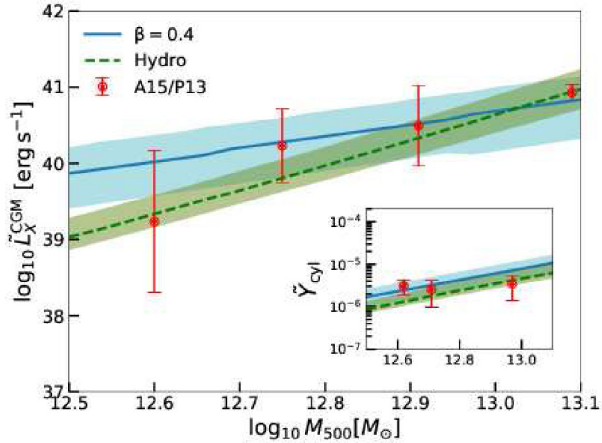
Figure 2. Stacked CGM soft X-ray luminosities and tSZ signal (inset) compared to the predictions of best-fitting parameter values (solid blue lines for power-law model and dashed green lines for the hydrostatic halo model). The shaded regions signify 68 per cent CL regions.

Figure 3. Hot CGM density profile for a Milky Way type-galaxy for the power-law model (blue solid line), the hydrostatic halo model (green dashed line), predictions by Fielding et al. 2017 (dot-dashed yellow line) and Fang et al. 2013 (long-dashed magenta line), and observations by Miller & Bregman 2015 (dotted red line) and Grcevich & Putman 2009 (grey points with error bars). The shaded regions represent the 68 per cent CL in the electron density determination.

drostatic model predicts larger X-ray luminosities. The power-law model also allows a larger uncertainty in the predicted signal owing to the larger uncertainties in the model parameters (see Table 2).

4 DISCUSSION

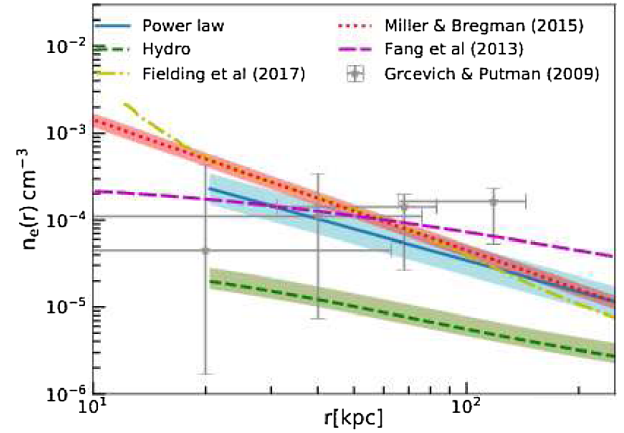### 4.1 Comparison with the hot halo of the Milky Way

The hot halo of the Milky Way has been studied in detail through a variety of methods (see Bland-Hawthorn & Gerhard 2016 for a recent review of the Milky Way observations). The best estimate of the virial mass of the Milky Way is $\sim 1.3 \times 10^{12}$ $M_\odot$ that translates to $M_{500} \sim 8.2 \times 10^{11}$ $M_\odot$. Therefore, the Milky Way lies below the lowest mass tSZ/X-ray data points used for our analysis. In Fig. 3, we extrapolate our best-fitting predictions for $M_v = 1.3 \times 10^{12}$ $M_\odot$ (at $r > 0.15 \times R_{500}$) and compare it with the observed density of the hot halo of the Milky Way from the following:

(i) The hot CGM density required to explain the observed ram pressure stripping of the dwarf satellites of the Milky Way from Grcevich & Putman (2009).

(ii) An adiabatic hot halo (assuming the hot gas to contain 10 per cent of the total halo mass, $M_v = 10^{12}$ $M_\odot$), shown to be consistent with a number of independent observations (Fang, Bullock & Boylan-Kolchin 2013).

(iii) CGM profile derived from *XMM–Newton* observations of OVII and OVIII emission lines along ~ 650 sightlines and OVII and OVIII absorption lines in the background quasar spectra, assuming a power-law model ($n_e \propto r^{-3\beta}$; Miller & Bregman 2015).

(iv) Results of a three-dimensional hydrodynamic simulations including stellar feedback, radiative cooling, and the cosmological accretion for a Milky Way- type galaxy with $M_{200} = 10^{12}$ $M_\odot$ (Fielding et al. 2017).

Note that, Miller & Bregman (2015) start with a β-model and core radius ~ 5 kpc, and then approximate it to a simple power-law form since only 4 of 649 OVII and OVIII emission lines pass through $r < 5$ kpc. Our best-fitting power-law model gives a hot gas mass $\sim 4.4^{+2.2}_{-1.5} \times 10^{10} M_\odot$ (~ 3.4 per cent of M_v), whereas the hydrostatic model predicts $\sim 9.0^{+3.6}_{-1.5} \times 10^9 M_\odot$ (~ 0.7 per cent of M_v), within 285 kpc. The hot gas mass predicted by our power-law model is much smaller than the value ($\sim 10^{11} M_\odot$ for $M_v = 10^{12}$ $M_\odot$) assumed by Fang et al. (2013). The hot CGM mass predicted by the β-model of Miller & Bregman (2015) is $\sim 6 \times 10^{10} M_\odot$ (within 285 kpc). Fielding et al. (2017) find that the CGM density distribution for $M_{200} \sim 10^{12}$ $M_\odot$ haloes is nearly independent of the variation in stellar feedback. Using their CGM density profiles, we find that the CGM mass is $\sim 3.7 \times 10^{10} M_\odot$, within 285 kpc. These mass estimates are within the 68 per cent CL of our power-law model, whereas our hydrostatic model predicts a much smaller hot CGM reservoir.

4.2 Comparison with other phases of CGM

The cool, warm, and the hot CGM are the three main phases of CGM that contribute significantly to the baryon census of the galaxy (see Tumlinson et al. 2017, their section 5.2, for a recent compilation). The mass budget of the cool CGM, best studied through low ions (CII, CIII, SiII, SiIII, MgII etc.) in the ultraviolet absorption line spectroscopy, is around $10^{10} - 10^{11}$ $M_\odot$ for low-redshift $L*$ galaxies (Werk et al. 2014; Stern et al. 2016; Prochaska et al. 2017). The mass budget of the warm CGM, traced by high ions (CIV, OIV etc.) has higher uncertainty due to the uncertainty in the ionization mechanism. For $L*$ galaxies, the warm CGM contains
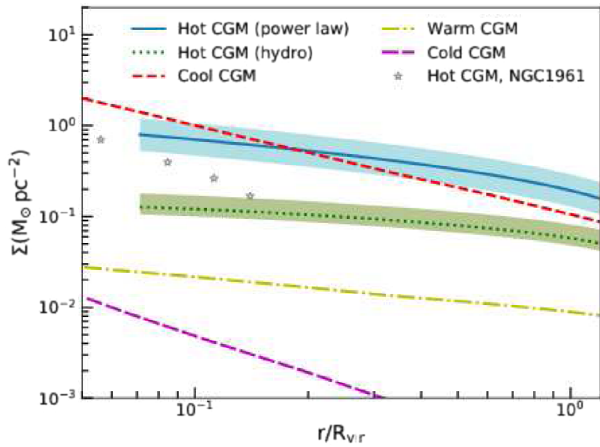
Figure 4. $_\mathrm{v}$Surface density profile of the hot CGM for the power-law model (solid blue line) and the hydrostatic halo model (dotted green line), cool CGM (dashed red line; Werk et al. 2014), warm CGM (dot-dashed yellow line; Tumlinson et al. 2011; Peeples et al. 2014), cold CGM (long-dashed magenta line; Zhu & Ménard 2013), and the hot CGM in NGC 1961 (grey points; Anderson, Churazov & Bregman 2016). Note that beyond $\approx 0.2R$, the hot CGM component in case of our power-law model dominates over all the other phases of the CGM.

$> 2 \times 10^9$ M$_\odot$ (Tumlinson et al. 2011). Our hot CGM mass estimate ($\sim 6 \times 10^9 - 7.5 \times 10^{10}$ M$_\odot$ for the two models at $M_\mathrm{v} \sim 1-2 \times 10^{12}$ M$_\odot$) is comparable to or larger than the mass contained in other CGM phases. Together the cool, warm, and the hot phases of CGM offer a potential solution to the galactic missing baryon problem.

In Fig. 4, we compare the surface density profile of the hot CGM (at $M_\mathrm{v} = 1.3 \times 10^{12}$ M$_\odot$ integrated out to $2R_\mathrm{v}$) with the profiles of other CGM phases (from fig. 7 of Tumlinson et al. 2017). Our power-law model for the hot component dominates the surface density at $r/R_\mathrm{v} > 0.2$, whereas the hydrostatic hot halo model is subdominant at all radii.

4.3 Impact of uncertainties

In this section, we estimate the robustness of our results to the uncertainties surrounding the fiducial parameters and observed signal:

(i) Uncertainties in the hot CGM temperature and metallicity: Our temperature profiles are normalized to give $f_{12} = 3.4$, i.e. $T_\mathrm{norm} = 2 \times 10^6$ K for a 10^{12} M$_\odot$ galaxy. These choices are motivated by the observations of the Milky Way and external galaxies with $M_\mathrm{v} \gtrsim 10^{12}$ M$_\odot$ (using spectral analysis of the inner halo $\lesssim 0.1-0.2$ R_v in case of external galaxies). Given the large scatter in the properties for individual spiral galaxies (Li et al. 2017; Anderson et al. 2013), we explore the impact of our choice of temperature and metallicity by changing the temperature normalization to $T_\mathrm{norm} \rightarrow T_\mathrm{norm}/2$ ($f_{12} = 1.7$) and $2 \times T_\mathrm{norm}$ ($f_{12} = 6.8$). Increasing (decreasing) the temperature normalization by a factor of two, results in a change in α_fg by ~ 8 per cent that leads to decrease (increase) of f_gas by 12.5 per cent (15 per cent), respectively, for 10^{12}M$_\odot$ haloes and a decrease (increase) of f_gas by 8 per cent (9 per cent), respectively, for 10^{13}M$_\odot$ haloes. The corresponding change in α_T is ~ 33 per cent, resulting in the change in the CGM temperature by roughly 30 per cent, either way for 10^{13}M$_\odot$ haloes. These effects are even smaller for the hydrostatic model. Instead of a fixed f_{12}, we also check to see its impact if left free as one extra parameter reflecting any unknown uncertainty in the temperature normalization. We find that using f_{12} as a free parameter with the

reasonable uniform prior in the range [1.7−6.8], i.e. a 100 per cent uncertainty in our fiducial normalization, has negligible effects on the resultant gas fraction and temperature.

We have further used a fixed metallicity of $0.2Z_\odot$ for all masses. Increasing Z= 0.2 to 0.4 Z$_\odot$ has negligible effects on the CGM temperature estimation, whereas there is a small decrease in the hot CGM fraction by a factor 1.5 for the power-law and 1.2 for the hydrostatic model.

(ii) Uncertainty in the stacked tSZ/X-ray signal: Our analysis assumes that P13 and A15 measurements represent the true one-halo term. However, a recent study by Vikram, Lidz & Jain (2017) points out that the two-halo term in SZ group cross-correlation function can dominate over the one-halo term in $M_\mathrm{v} \lesssim 10^{13}$ M$_\odot$ haloes. P13 avoid the two-halo contribution to Y_{500} by applying certain isolation criteria (see P13 for details) to their galaxy catalogue .[5] The stacked tSZ signal is also marginally detected at halo masses $M_{500} < 10^{13}$ M$_\odot$. Wang et al. (2016) used almost the same sample of LBGs to measure the stacked weak gravitational lensing signal. Their estimated effective halo mass, for a given stellar mass bin, is lower compared to P13/A15 results. This shift in halo mass is equivalent to 30 per cent increase in tSZ signal and 40 per cent increase in X-ray signal, which can lead to a larger hot CGM content.

Incorporating the above uncertainties in our analysis is beyond the scope of this paper. However, to bypass our lack of understanding of the tSZ signal, we estimate the hot CGM content using X-ray data only. For the power-law density profile, X-ray emission alone gives $\alpha_\mathrm{fg} = 0.29^{+0.07}_{-0.03}$ and $\alpha_T = -0.1 \pm 0.6$. While α_T is unconstrained as expected, the constraint on α_fg agrees with the joint X-ray–tSZ constraint within 1σ. For the hydrostatic model, both the parameters are poorly constrained ($\alpha_\mathrm{fg} = 0.34^{+0.30}_{-0.27}$, $\alpha_T = -0.11 \pm 0.38$) since the temperature uncertainties feed into the density estimation.

5 SUMMARY

We have obtained the joint X-ray–tSZ constraints on the hot CGM mass fraction and temperature for massive galaxies. The data sets used in this paper are from P13 (stacked tSZ) and A15 (stacked X-ray luminosity). The two CGM density profiles considered here, namely the power-law and the hydrostatic halo model, are based on the assumptions that (1) the gas is isothermal, (2) the gas temperature at $M_\mathrm{v} = 10^{12}$ M$_\odot$ is $\sim 2 \times 10^6$ K, and (3) a uniform metallicity, 0.2 Z$_\odot$. The main conclusions of this work are the following:

(i) The power-law model predicts $f_\mathrm{gas} \sim 3.2^{+1.7}_{-1.1}$ per cent and $5.5^{+1.8}_{-1.4}$ per cent for the halo masses 10^{12} and 10^{13}M$_\odot$, respectively. Therefore, the hot CGM holds approximately 20–30 per cent of baryonic mass in massive haloes. The predicted gas temperature at $M_\mathrm{v} = 10^{13}$ M$_\odot$ is $\sim 0.21^{+0.04}_{-0.05}$ keV, only slightly larger than the temperature at $M_\mathrm{v} = 10^{12}$ M$_\odot$ (0.17 keV).

(ii) The hydrostatic halo model predicts lower hot gas fractions ($0.6^{+0.3}_{-0.1}$ per cent and $1.8^{+0.5}_{-0.2}$ per cent at $M_\mathrm{v} = 10^{12}$ and 10^{13} M$_\odot$, respectively) and higher temperatures ($T_\mathrm{gas} \sim 0.38^{+0.05}_{-0.02}$ keV at $M_\mathrm{v} = 10^{13}$M$_\odot$) compared to the power-law model. This translates to a baryon budget of 4–11 per cent.

(iii) Extrapolating the density profiles to $2R_\mathrm{v}$ increases the baryon budget in the hot CGM to 46 (78) per cent for the power-law model and 13 (24) per cent for the hydrostatic hot halo model at $M_\mathrm{v} = 10^{12}$ (10^{13}) M$_\odot$. Note that a recent study by Lim et al. (2017) stacked

---

[5]However, Hill et al. (2017) argue that the isolation criteria used by P13 are not robust for low-mass haloes.

the kinetic (SZ) signal from galaxy groups down to the halo mass $\sim 10^{12.3}$ M$_\odot$ and showed that their results are consistent with the CGM containing galactic cosmic baryon fraction in the warm phase ($T_{\rm eff} \sim 10^5 - 10^6$ K) within the virial radius of the galaxy, however with large uncertainties in the CGM mass fraction. They use a β-profile (with $\beta = 0.86$) to extract the signal within $3R_{500}$ and use the same profile to obtain the signal within R_{500}. However, such conversions are sensitive to the assumed density profile (see Section 2.1) and may result in the overestimation of the signal, especially for low-mass haloes.

(iv) The predictions of the power-law model (extrapolated to $M_{\rm v} \sim 1.3 \times 10^{12}$ M$_\odot$) are in agreement with the observations of the Milky Way, whereas the hydrostatic model predicts a low-density and hot gas fraction. Our estimate of the hot CGM mass is comparable to or larger than the mass predicted in other phases (cool and warm phases) of the CGM in $L*$ galaxies.

(v) Relaxing our assumptions about the gas temperature and metallicities around their fiducial values have only small effects on the best-fitting values of the model parameters, given the uncertainties in these parameters.

(vi) It is difficult to explore the variations in β, the temperature profile, and gas metallicity across the mass range due to the paucity of data in this mass range. Additionally, the observations of the hot CGM in individual massive galaxies are limited to 10–20 per cent of $R_{\rm v}$. A large fraction of the hot CGM is expected to be distributed out to the virial radius, making it difficult to directly compare them with our results. The situation is expected to improve with more observations in future.

ACKNOWLEDGEMENTS

REFERENCES

Anderson M. E., Bregman J. N., 2010, ApJ, 714, 320
Anderson M. E., Bregman J. N., 2011, ApJ, 737, 22
Anderson M. E., Bregman J. N., Dai X., 2013, ApJ, 762, 106
Anderson M. E., Gaspari M., White S. D. M., Wang W., Dai X., 2015, MNRAS, 449, 3806
Anderson M. E., Churazov E., Bregman J. N., 2016, MNRAS, 455, 227
Arnaud M., Pratt G. W., Piffaretti R., Böhringer H., Croston J. H., Pointecouteau E., 2010, A&A, 517, A92
Bell E. F., McIntosh D. H., Katz N., Weinberg M. D., 2003, ApJ, 585, L117
Bland-Hawthorn J., Gerhard O., 2016, ARA&A, 54, 529
Blanton M. R., Roweis S., 2007, AJ, 133, 734
Crain R. A., McCarthy I. G., Frenk C. S., Theuns T., Schaye J., 2010, MNRAS, 407, 1403

Dai X., Anderson M. E., Bregman J. N., Miller J. M., 2012, ApJ, 755, 107
Duffy A. R., Battye R. A., Davies R. D., Moss A., Wilkinson P. N., 2008, MNRAS, 383, 150
Fang T., Bullock J., Boylan-Kolchin M., 2013, ApJ, 762, 20
Fielding D., Quataert E., McCourt M., Thompson T. A., 2017, MNRAS, 466, 3810
Flynn C., Holmberg J., Portinari L., Fuchs B., Jahreiß H., 2006, MNRAS, 372, 1149
Foreman-Mackey D., Hogg D. W., Lang D., Goodman J., 2013, PASP, 125, 306
Gatto A., Fraternali F., Read J. I., Marinacci F., Lux H., Walch S., 2013, MNRAS, 433, 2749
Grcevich J., Putman M. E., 2009, ApJ, 696, 385
Greco J. P., Hill J. C., Spergel D. N., Battaglia N., 2015, ApJ, 808, 151
Guo Q., White S., Angulo R. E., Henriques B., Lemson G., Boylan-Kolchin M., Thomas P., Short C., 2013, MNRAS, 428, 1351
Hill J. C., Baxter E. J., Lidz A., Greco J. P., Jain B., 2017
Kereš D., Katz N., Weinberg D. H., Davé R., 2005, MNRAS, 363, 2
Klypin A., Zhao H., Somerville R. S., 2002, ApJ, 573, 597
Le Brun A. M. C., McCarthy I. G., Melin J.-B., 2015, MNRAS, 451, 3868
Li J.-T., Bregman J. N., Wang Q. D., Crain R. A., Anderson M. E., Zhang S., 2017, ApJS, 233, 20
Lim S., Mo H., Wang H., Yang X., 2017
Maller A. H., Bullock J. S., 2004, MNRAS, 355, 694
McGaugh S. S., Schombert J. M., de Blok W. J. G., Zagursky M. J., 2010, ApJ, 708, L14
Miller M. J., Bregman J. N., 2015, ApJ, 800, 14
Peeples M. S., Werk J. K., Tumlinson J., Oppenheimer B. D., Prochaska J. X., Katz N., Weinberg D. H., 2014, ApJ, 786, 54
Planck Collaboration XI, 2013, A&A, 557, A52
Prochaska J. X. et al., 2017, ApJ, 837, 169
Rees M. J., Ostriker J. P., 1977, MNRAS, 179, 541
Sharma P., McCourt M., Parrish I. J., Quataert E., 2012, MNRAS, 427, 1219
Silk J., 1977, ApJ, 211, 638
Singh P., Nath B. B., Majumdar S., Silk J., 2015, MNRAS, 448, 2384
Singh P., Majumdar S., Nath B. B., Refregier A., Silk J., 2016, MNRAS, 456, 1495
Smith R. K., Brickhouse N. S., Liedahl D. A., Raymond J. C., 2001, ApJ, 556, L91
Springel V. et al., 2005, Nature, 435, 629
Stern J., Hennawi J. F., Prochaska J. X., Werk J. K., 2016, ApJ, 830, 87
Tumlinson J. et al., 2011, Science, 334, 948
Tumlinson J., Peeples M. S., Werk J. K., 2017, ARA&A, 55, 389
Vikram V., Lidz A., Jain B., 2017, MNRAS, 467, 2315
Wang W., White S. D. M., Mandelbaum R., Henriques B., Anderson M. E., Han J., 2016, MNRAS, 456, 2301
Werk J. K. et al., 2014, ApJ, 792, 8
White S. D. M., Frenk C. S., 1991, ApJ, 379, 52
Zhu G., Ménard B., 2013, ApJ, 770, 130

This paper has been typeset from a TEX/LATEX file prepared by the author.